PHYSICS OF FLUIDS **26**, 032001 (2014)

On the damping effect of gas rarefaction on propagation of acoustic waves in a microchannel

A. Manela,[1,a)] G. A. Radtke,[2] and L. Pogorelyuk[1]
[1]*Faculty of Aerospace Engineering, Technion - Israel Institute of Technology, Haifa 32000, Israel*
[2]*Sandia National Laboratories, P.O. Box 5800, Albuquerque, New Mexico 87185, USA*

(Received 10 September 2013; accepted 10 February 2014; published online 5 March 2014)

We consider the response of a gas in a microchannel to instantaneous (small-amplitude) non-periodic motion of its boundaries in the normal direction. The problem is formulated for an ideal monatomic gas using the Bhatnagar, Gross, and Krook (BGK) kinetic model, and solved for the entire range of Knudsen (Kn) numbers. Analysis combines analytical (collisionless and continuum-limit) solutions with numerical (low-variance Monte Carlo and linearized BGK) calculations. Gas flow, driven by motion of the boundaries, consists of a sequence of propagating and reflected pressure waves, decaying in time towards a final equilibrium state. Gas rarefaction is shown to have a "damping effect" on equilibration process, with the time required for equilibrium shortening with increasing Kn. Oscillations in hydrodynamic quantities, characterizing gas response in the continuum limit, vanish in collisionless conditions. The effect of having two moving boundaries, compared to only one considered in previous studies of time-periodic systems, is investigated. Comparison between analytical and numerical solutions indicates that the collisionless description predicts the system behavior exceptionally well for all systems of the size of the mean free path and somewhat larger, in cases where boundary actuation acts along times shorter than the ballistic time scale. The continuum-limit solution, however, should be considered with care at early times near the location of acoustic wavefronts, where relatively sharp flow-field variations result in effective increase in the value of local Knudsen number. [http://dx.doi.org/10.1063/1.4866443]

I. INTRODUCTION

Continuum investigations of propagation of sound waves in a gas is a classical problem in fluid dynamics, which has been studied extensively over the years.[1] Inevitably, these studies are based on the dual assumption that characteristic time and length scales of the problem are much larger than the mean free time and mean free path of a gas molecule, respectively. In cases where one of these conditions fails, continuum description breaks down and cannot be applied. Such conditions are common, for example, in high-frequency sound (with frequency of the order of collision frequency), or in micro-size and near-vacuum systems, where the physical length-scale is comparable to the molecular mean free path. These and other applications have motivated the study of sound wave propagation in rarefied gases.

Starting from the pioneering investigations of Greenspan[2] and Meyer and Sessler[3] in the 1950s, theoretical and experimental studies on sound propagation in non-continuum conditions have evolved throughout the second half of the 20th century and continued through to current research.[4–17] Initially, theoretical investigations have concentrated on studying sound propagation in semi-infinite geometries, where a moving boundary has acted as a "sound source" (e.g., Refs. 8, 11, and 14). Later contributions have studied the problem in a confined setup, by adding a stationary boundary to

[a)]Author to whom correspondence should be addressed. Electronic address: amanela@technion.ac.il.

act as a "resting receiver," and examined the impact of sound-wave reflections.[15–17] While the large majority of works have considered the linearized problem of small-amplitude boundary motion, few analyses have also examined the nonlinear regime of large-amplitude wave propagation (e.g., Ref. 18).

Common to all of the above works is the prescription of *harmonic* time-dependence of the moving boundary velocity. Consequently, the system response was always assumed time-periodic, and only the space variation of flow-field properties has been considered. Recently, Tsuji and Aoki[19] have considered a nonlinear time-dependent problem of a passive plate-on-a-spring setup interacting with a semi-infinite gas expanse. The work has concentrated on analyzing numerical discontinuities appearing in the numerical solution for the probability density function, and quantified the decay rate of plate oscillations due to gas-structure interactions. As this is the only occasion where time-dependent acoustic equilibration has been investigated, much work is still needed to analyze the approach to acoustic relaxation in a rarefied medium. The main purpose of the present contribution is to extend previous investigations by analyzing the system response to *arbitrary non-periodic* boundary actuation in a confined domain, both analytically and numerically. Specifically, this is important for two main reasons: first, acoustic wave propagation does not necessarily result from periodic boundary actuation, and it is of practical interest to analyze system response to non-periodic excitation; second, such an investigation should reveal the transient response of the gas, and shed light on the effect of gas rarefaction on relaxation processes.

We consider a linearized setup of a gas confined in an infinitely long microchannel and subject to prescribed small-amplitude boundary actuation. Taking a non-periodic "bump-like" boundary velocity profile, the system response is analyzed in the entire range of gas rarefaction conditions, using the framework of kinetic theory of gases. In Sec. II, the general problem is formulated using the Bhatnagar, Gross, and Krook (BGK) kinetic model[20] of the Boltzmann equation. The problem is analyzed analytically and numerically in Secs. III and IV. Results are presented and discussed in Sec. V. Concluding comments are given in Sec. VI, where the effect of replacing the BGK model with a different (hard-sphere) model of molecular interaction is discussed. Some technical details are relegated to the Appendix.

II. PROBLEM STATEMENT

Consider a monatomic gas layer of uniform density ρ_0^* confined between two parallel infinitely long diffusely reflecting walls placed at $x^* = \mp L^*/2$ (here asterisks denote dimensional quantities). The gas is initially at rest and in thermodynamic equilibrium with the isothermal boundaries, which are kept at a temperature T_0^*. At time $t^* \geq 0$, one or both walls move in the normal direction into the gas layer according to a prescribed (arbitrary) small-amplitude profile,

$$\varepsilon \mathbf{U}_{w_\pm}^*(t^*) = \varepsilon U_{w_\pm}^*(t^*)\hat{\mathbf{x}}, \tag{1}$$

with "plus" and "minus" signs corresponding to the motion of walls located at $x^* = -L^*/2$ and $x^* = +L^*/2$, respectively. Here, $\varepsilon \ll 1$ so that total walls motion is small compared to L^* and the system description may be linearized about its initial equilibrium.

To render the problem dimensionless, we normalize position, velocity, and time by L^*, $U_{th}^* = \sqrt{2R^*T_0^*}$ (marking the mean thermal speed of gas molecules, with R^* denoting the specific gas constant), and acoustic time-scale $t_a^* = L^*/U_{th}^*$, respectively. Density and temperature are scaled by ρ_0^* and T_0^*, respectively. In the framework of kinetic theory of gases, the gas state is described by the velocity distribution function,

$$f(x, t, \mathbf{c}) = F[1 + \varepsilon\phi(x, t, \mathbf{c})], \tag{2}$$

wherein $\mathbf{c} = (c_x, c_y, c_z)$ is the vector of molecular velocity, and $F = \pi^{-3/2}\exp[-c^2]$ is the equilibrium Maxwellian distribution. Adopting the kinetic BGK model,[20] and linearizing the problem about its initial equilibrium, we obtain a linearized equation for $\phi(t, x, \mathbf{c})$,

$$\frac{\partial\phi}{\partial t} + c_x\frac{\partial\phi}{\partial x} = \frac{2}{\sqrt{\pi}Kn}\left[\rho + 2c_x u + \left(c^2 - \frac{3}{2}\right)T - \phi\right]. \tag{3}$$

In (3), Kn denotes the Knudsen number,

$$Kn = l^*/L^*, \tag{4}$$

with l^* marking the mean free path of a gas molecule. Density, x-direction velocity, and temperature perturbations are denoted by ρ, u, and T, respectively, and are expressed via ϕ through the molecular-velocity-space quadratures[21]

$$\rho(x,t) = \frac{1}{\pi^{3/2}} \int_{-\infty}^{\infty} \phi \exp\left[-c^2\right] \mathrm{d}\mathbf{c}, \tag{5}$$

$$u(x,t) = \frac{1}{\pi^{3/2}} \int_{-\infty}^{\infty} c_x \phi \exp\left[-c^2\right] \mathrm{d}\mathbf{c}, \tag{6}$$

and

$$T(x,t) = \frac{1}{\pi^{3/2}} \int_{-\infty}^{\infty} \left(\frac{2}{3}c^2 - 1\right) \phi \exp\left[-c^2\right] \mathrm{d}\mathbf{c}. \tag{7}$$

In accordance with the linearized form of equation of state for an ideal gas, pressure perturbation is given by

$$p(x,t) = \rho(x,t) + T(x,t), \tag{8}$$

where the pressure is normalized by $\rho_0^* R^* T_0^*$. The problem is supplemented by imposing an initial condition,

$$\phi(x, t = 0^-, \mathbf{c}) = 0, \tag{9}$$

together with linearized diffuse boundary conditions at the walls,

$$\phi(x = \mp 1/2, t, c_x \gtrless 0) = \rho_{\pm}(t) + 2c_x U_{w_{\pm}}(t). \tag{10}$$

In (10), $U_{w_{\pm}}(t)$ are prescribed functions obtained from the scaled form of (1), and $\rho_{\pm}(t)$ are yet to be determined. Equations (3)–(7), (9), and (10) complete the formulation of the problem analyzed in the succeeding section.

III. ANALYSIS

The problem formulated in Sec. II is analyzed in the ballistic ($Kn \gg 1$, Sec. III A) and continuum ($Kn \ll 1$, Sec. III C) limits. A general scheme for numerical solution at arbitrary Kn is constructed in Sec. III B.

A. Ballistic flow limit

In the ballistic $Kn \gg 1$ limit of no molecular collisions, the linearized problem for ϕ consists of the collisionless Boltzmann equation

$$\frac{\partial \phi}{\partial t} + c_x \frac{\partial \phi}{\partial x} = 0, \tag{11}$$

together with initial and boundary conditions (9) and (10). Taking the Laplace transform of (11) and making use of (9) and (10) yield the solution

$$\hat{\phi}(s, x, c_x \gtrless 0, c_y, c_z) = \left[\hat{\rho}_{\pm}(s) + 2c_x \hat{U}_{w_{\pm}}(s)\right] \exp\left[-\frac{s}{c_x}\left(x \pm \frac{1}{2}\right)\right], \tag{12}$$

where s is the Laplace variable and $\hat{}$ denotes the Laplace transform of a function. By inversion of (12), we obtain

$$\phi(t, x, c_x \gtrless 0, c_y, c_z) = \rho_{\pm}(t_{\pm}) + 2c_x U_{w_{\pm}}(t_{\pm}), \tag{13}$$

where $t_\pm = t - (x \pm 1/2)/c_x$. The fields $\rho_\pm(t)$ are determined by imposing no-penetration conditions at the walls,

$$\frac{1}{\pi^{3/2}} \int_{-\infty}^{\infty} c_x \phi \left(x = \mp \frac{1}{2} \right) \exp(-c^2) d\mathbf{c} = U_{w_\pm}(t). \tag{14}$$

Substituting (13) into (14), and following the derivation outlined in the Appendix, yield a pair of coupled integral equations,

$$\rho_+(t) - \rho_-(0) \exp\left[-\frac{1}{t^2}\right] - \int_0^t \frac{\mathrm{d}\rho_-}{\mathrm{d}\tau} \exp\left[-\frac{1}{(t-\tau)^2}\right] d\tau = \sqrt{\pi} U_{w_+}(t) - 4 \int_0^t \frac{U_{w_-}(\tau)}{(t-\tau)^4} \exp\left[-\frac{1}{(t-\tau)^2}\right] d\tau \tag{15}$$

and

$$\rho_-(t) - \rho_+(0) \exp\left[-\frac{1}{t^2}\right] - \int_0^t \frac{\mathrm{d}\rho_+}{\mathrm{d}\tau} \exp\left[-\frac{1}{(t-\tau)^2}\right] d\tau = -\sqrt{\pi} U_{w_-}(t) + 4 \int_0^t \frac{U_{w_+}(\tau)}{(t-\tau)^4} \exp\left[-\frac{1}{(t-\tau)^2}\right] d\tau, \tag{16}$$

to be solved in conjunction with the initial conditions $\rho_\pm(0) = \pm\sqrt{\pi} U_{w_\pm}(0)$. Rewriting the problem in terms of $\sigma = \rho_+ + \rho_-$ and $\delta = \rho_+ - \rho_-$ results in two decoupled equations,

$$\sigma(t) - \int_0^t \frac{\mathrm{d}\sigma}{d\tau} \exp\left[-\frac{1}{(t-\tau)^2}\right] d\tau = \sqrt{\pi} \left[U_\sigma(0) \exp\left[-\frac{1}{t^2}\right] + U_\sigma(t) \right] + 4 \int_0^t \frac{U_\sigma(\tau)}{(t-\tau)^4} \exp\left[-\frac{1}{(t-\tau)^2}\right] d\tau \tag{17}$$

and

$$\delta(t) - \int_0^t \frac{\mathrm{d}\delta}{d\tau} \exp\left[-\frac{1}{(t-\tau)^2}\right] d\tau = \sqrt{\pi} \left[U_\delta(0) \exp\left[-\frac{1}{t^2}\right] + U_\delta(t) \right] - 4 \int_0^t \frac{U_\delta(\tau)}{(t-\tau)^4} \exp\left[-\frac{1}{(t-\tau)^2}\right] d\tau, \tag{18}$$

supplemented by the initial conditions $\sigma(0) = \sqrt{\pi} U_\sigma(0)$ and $\delta(0) = \sqrt{\pi} U_\delta(0)$. Here, $U_\sigma = U_{w_+} + U_{w_-}$ and $U_\delta = U_{w_+} - U_{w_-}$.

The above initial-value problems for σ and δ are solved numerically, for an arbitrary choice of $U_{w_\pm}$, using a simple Euler-type method. Towards this end, we formulate Eqs. (17) and (18) in the general form

$$F(t) - k_1 \int_0^t \frac{\mathrm{d}F}{\mathrm{d}\tau} \exp\left[-\frac{1}{(t-\tau)^2}\right] \mathrm{d}\tau = G(t), \tag{19}$$

with $F(t)$ denoting either $\sigma(t)$ or $\delta(t)$, and $F(0) = k_2$ (constants k_1 and k_2 are determined from Eqs. (17) and (18), respectively). Discretizing the time using a time-step series $t_{n+1} = t_n + \Delta t$, we make use of a linearized Taylor approximation,

$$F(t_{n+1}) \approx F(t_n) + \left(\frac{\mathrm{d}F}{\mathrm{d}t} \right)_{t_n} \Delta t, \tag{20}$$

to carry out a time-step integration. To obtain an expression for $(\mathrm{d}F/\mathrm{d}t)_{t_n}$, we evaluate the integral term in Eq. (19) via

$$\int_0^{t_n} \frac{\mathrm{d}F}{\mathrm{d}\tau} \exp\left[-\frac{1}{(t_n-\tau)^2}\right] \mathrm{d}\tau \approx \left(\frac{\mathrm{d}F}{\mathrm{d}t} \right)_{t_0=0} \int_0^{t_1} \exp\left[-\frac{1}{(t_n-\tau)^2}\right] \mathrm{d}\tau + \cdots + \left(\frac{\mathrm{d}F}{\mathrm{d}t} \right)_{t_{n-1}} \int_{t_{n-1}}^{t_n} \exp\left[-\frac{1}{(t_n-\tau)^2}\right] \mathrm{d}\tau. \tag{21}$$

Substituting (21) into (19) and collecting terms yield an explicit expression for $(\mathrm{d}F/\mathrm{d}t)_{t_n}$,

$$\left(\frac{\mathrm{d}F}{\mathrm{d}t}\right)_{t_n} \approx \frac{G(t_{n+1}) - F(t_n) + k_1 \sum_{j=0}^{n-1} \left(\frac{\mathrm{d}F}{\mathrm{d}t}\right)_{t_j} \int_{t_j}^{t_{j+1}} \exp\left[-\frac{1}{(t_{n+1}-\tau)^2}\right] \mathrm{d}\tau}{\Delta t - k_1 \int_{t_n}^{t_{n+1}} \exp\left[-\frac{1}{(t_{n+1}-\tau)^2}\right] \mathrm{d}\tau}, \tag{22}$$

which is then substituted into (20) to calculate $F(t_{n+1})$. While the above scheme is accurate to only first order (and thus facilitates numerical implementation), the comparison carried out in Sec. V demonstrates its effectiveness in providing an accurate solution to Eqs. (17) and (18).

Once solutions for $\sigma(t)$ and $\delta(t)$ are obtained, $\rho_\pm$ are known (through $\rho_\pm = (\sigma \pm \delta)/2$), and the probability density function perturbation ϕ in (13) is found. Making use of ϕ, the $O(\varepsilon)$ perturbations of the hydrodynamic fields are computed by appropriate quadratures over the molecular velocity space (see Eqs. (5)–(7)). Introducing

$$I_\pm^n = \int_0^t \frac{(x \pm 1/2)^{n+1}}{(t-\tau)^{n+2}} U_{w_\pm}(\tau) \exp\left[-\left(\frac{x \pm 1/2}{t-\tau}\right)^2\right] \mathrm{d}\tau$$

$$\text{and} \quad J_\pm^n = \int_0^t \frac{(x \pm 1/2)^{n+1}}{(t-\tau)^{n+2}} \rho_\pm(\tau) \exp\left[-\left(\frac{x \pm 1/2}{t-\tau}\right)^2\right] \mathrm{d}\tau, \tag{23}$$

the $O(\varepsilon)$ density, x-component velocity and pressure perturbations are expressed as

$$\rho = \frac{1}{\sqrt{\pi}} \left[J_+^0 - J_-^0 + 2\left(I_+^1 - I_-^1\right)\right], \tag{24}$$

$$u = \frac{1}{\sqrt{\pi}} \left[J_+^1 - J_-^1 + 2\left(I_+^2 - I_-^2\right)\right], \tag{25}$$

and

$$p = \frac{2}{3\sqrt{\pi}} \left[J_+^2 - J_-^2 + J_+^0 - J_-^0 + 2\left(I_+^3 - I_-^3 + I_+^1 - I_-^1\right)\right],$$

respectively. The temperature perturbation is obtained from the linearized gas equation of state (8),

$$T = p - \rho. \tag{26}$$

B. Solution for arbitrary Knudsen numbers

For arbitrary values of Kn, the solution to the problem is obtained by taking the time-Fourier transform of Eqs. (3)–(7), (9), and (10). Applying the Fourier transform of a function,

$$\bar{Q}(\omega) = \int_{-\infty}^{\infty} Q(t) \exp\left[-\mathrm{i}\omega t\right] \mathrm{d}t, \tag{27}$$

to the system of equations yields the transformed equation,

$$c_x \frac{\mathrm{d}\bar{\phi}}{\mathrm{d}x} + \left(\mathrm{i}\omega + \frac{2}{\sqrt{\pi}Kn}\right)\bar{\phi} = \frac{2}{\sqrt{\pi}Kn}\left[\bar{\rho} + 2c_x\bar{u} + \left(c^2 - \frac{3}{2}\right)\bar{T}\right], \tag{28}$$

together with the boundary conditions

$$\bar{\phi}(x = \mp 1/2, \omega, c_x \gtrless 0) = \bar{\rho}_\pm(\omega) + 2c_x \bar{U}_{w_\pm}(\omega). \tag{29}$$

The fields $\bar{\rho}_\pm(\omega)$ are determined by applying no-penetration condition at the walls, $u(x = \mp 1/2, t) = U_{w_\pm}(t)$, in the frequency domain. Making use of Eq. (29) in conjunction with the kinetic definition (6) of macroscopic gas velocity, we obtain an integral expression for $\bar{\rho}_\pm$,

$$\bar{\rho}_\pm(\omega) = \pm\sqrt{\pi}\bar{U}_{w_\pm}(\omega) \mp \frac{2}{\pi} \int_{c_x \lessgtr 0} c_x \bar{\phi}(x = \mp 1/2) \exp\left[-c^2\right] \mathrm{d}\mathbf{c}. \tag{30}$$

Numerical solution for the boundary-value problem (28)–(30) follows the scheme outlined in Ref. 15, and is recapitulated here for completeness. Defining

$$\bar{\psi}_1(x,\omega,c_x)=\frac{1}{\pi}\int_{-\infty}^{\infty}\bar{\phi}\exp\left[-c_y^2-c_z^2\right]\mathrm{d}c_y\mathrm{d}c_z \tag{31}$$

and

$$\bar{\psi}_2(x,\omega,c_x)=\frac{1}{\pi}\int_{-\infty}^{\infty}\left(c_y^2+c_z^2-1\right)\bar{\phi}\exp\left[-c_y^2-c_z^2\right]\mathrm{d}c_y\mathrm{d}c_z, \tag{32}$$

and carrying out appropriate c_y and c_z integrations of Eq. (28) yield a pair of coupled equations for $\bar{\psi}_1$ and $\bar{\psi}_2$,

$$c_x\frac{\mathrm{d}\bar{\psi}_1}{\mathrm{d}x}+\left(\mathrm{i}\omega+\frac{2}{\sqrt{\pi}Kn}\right)\bar{\psi}_1=\frac{2}{\sqrt{\pi}Kn}\left[\bar{\rho}+2c_x\bar{u}+\left(c_x^2-\frac{1}{2}\right)\bar{T}\right] \tag{33}$$

and

$$c_x\frac{\mathrm{d}\bar{\psi}_2}{\mathrm{d}x}+\left(\mathrm{i}\omega+\frac{2}{\sqrt{\pi}Kn}\right)\bar{\psi}_2=\frac{2}{\sqrt{\pi}Kn}\bar{T}, \tag{34}$$

where the transformed hydrodynamic fields are expressed via $\bar{\psi}_1$ and $\bar{\psi}_2$ through

$$\bar{\rho}(x,\omega)=\frac{1}{\sqrt{\pi}}\int_{-\infty}^{\infty}\bar{\psi}_1\exp\left[-c_x^2\right]\mathrm{d}c_x, \tag{35}$$

$$\bar{u}(x,\omega)=\frac{1}{\sqrt{\pi}}\int_{-\infty}^{\infty}c_x\bar{\psi}_1\exp\left[-c_x^2\right]\mathrm{d}c_x, \tag{36}$$

and

$$\bar{T}(x,\omega)=\frac{1}{\sqrt{\pi}}\int_{-\infty}^{\infty}\left(\frac{2}{3}c_x^2-\frac{1}{3}\right)\bar{\psi}_1\exp\left[-c_x^2\right]\mathrm{d}c_x+\frac{2}{3\sqrt{\pi}}\int_{-\infty}^{\infty}\bar{\psi}_2\exp\left[-c_x^2\right]\mathrm{d}c_x. \tag{37}$$

Applying a similar procedure to Eq. (29) yields the required boundary conditions for $\bar{\psi}_1$,

$$\bar{\psi}_1(x=\mp1/2,\omega,c_x\gtrless0)=\bar{\rho}_\pm(\omega)+2c_x\bar{U}_{w_\pm}(\omega), \tag{38}$$

and $\bar{\psi}_2$,

$$\bar{\psi}_2(x=\mp1/2,\omega,c_x\gtrless0)=0, \tag{39}$$

where the fields $\bar{\rho}_\pm(\omega)$ are given by

$$\bar{\rho}_\pm(\omega)=\pm\sqrt{\pi}\bar{U}_{w_\pm}(\omega)\mp\frac{2}{\pi}\int_{c_x\lessgtr0}c_x\bar{\psi}_1(x=\mp1/2)\exp\left[-c_x^2\right]\mathrm{d}c_x. \tag{40}$$

Numerical solution to the above problem is further simplified by separating $\bar{\psi}_1$ into

$$\bar{\psi}_1=\bar{\psi}_{1_a}+\bar{\psi}_{1_b}, \tag{41}$$

where $\bar{\psi}_{1_a}$ satisfies

$$c_x\frac{\mathrm{d}\bar{\psi}_{1_a}}{\mathrm{d}x}+\left(\mathrm{i}\omega+\frac{2}{\sqrt{\pi}Kn}\right)\bar{\psi}_{1_a}=0, \tag{42}$$

with boundary conditions

$$\bar{\psi}_{1_a}(x=\mp1/2,\omega,c_x\gtrless0)=\bar{\rho}_{a_\pm}(\omega)+2c_x\bar{U}_{w_\pm}(\omega), \tag{43}$$

and

$$\bar{\rho}_{a_\pm}(\omega)=\pm\sqrt{\pi}\bar{U}_{w_\pm}(\omega)\mp2\int_{c_x\lessgtr0}c_x\bar{\psi}_{1_a}(x=\mp1/2)\exp\left[-c_x^2\right]\mathrm{d}c_x, \tag{44}$$

and $\bar{\psi}_{1_b}$ satisfies

$$c_x \frac{\mathrm{d}\bar{\psi}_{1_b}}{\mathrm{d}x} + \left(\mathrm{i}\omega + \frac{2}{\sqrt{\pi}Kn}\right)\bar{\psi}_{1_b} = \frac{2}{\sqrt{\pi}Kn}\left[\bar{\rho} + 2c_x\bar{u} + \left(c_x^2 - \frac{1}{2}\right)\bar{T}\right], \tag{45}$$

with conditions

$$\bar{\psi}_{1_b}(x = \mp 1/2, \omega, c_x \gtrless 0) = \bar{\rho}_{b_\pm}(\omega), \tag{46}$$

and

$$\bar{\rho}_{b_\pm}(\omega) = \mp 2\int_{c_x \lessgtr 0} c_x \bar{\psi}_{1_b}(x = \mp 1/2), \exp\left[-c_x^2\right] \mathrm{d}c_x. \tag{47}$$

The solution for $\bar{\psi}_{1_a}$ can be expressed in a closed form,

$$\bar{\psi}_{1_a} = \left[\bar{\rho}_{a_\pm}(\omega) + 2c_x\bar{U}_{w_\pm}(\omega)\right]\exp\left[-\frac{x \pm 1/2}{c_x}\, z\right], \; c_x \gtrless 0, \tag{48}$$

where $z = \mathrm{i}\omega + 2/(\pi^{1/2}Kn)$, and

$$\bar{\rho}_{a_\pm}(\omega) = \frac{\pm 1}{1 - 4S_1^2(z)}\left[\bar{U}_{w_\pm}(\omega)\left(\sqrt{\pi} + 8S_1(z)S_2(z)\right) - 2\bar{U}_{w_\pm}(\omega)\left(\sqrt{\pi}S_1(z) + 2S_2(z)\right)\right]. \tag{49}$$

In (49),

$$S_n(z) = \int_0^\infty p^n \exp\left[-\frac{z}{p} - p^2\right] \mathrm{d}p.$$

It is worthwhile to note that the ballistic-flow solution, derived independently in Sec. III A using a Laplace-transform technique, can be calculated from taking the inverse Fourier transform (see (50)) of $\bar{\psi}_{1_a}$ in (48) in the limit $Kn \to \infty$. Yet, apart from being more efficient for numerical implementation, the Laplace-transform approach has the advantage of not requiring explicit knowledge of the Fourier transform of the actuating signal $U_{w_\pm}(t)$.

The frequency-domain solution is completed via numerical integration of the problems for $\bar{\psi}_{1_b}$ and $\bar{\psi}_2$. Towards this end, Eqs. (34)–(37), (39), and (45)–(47) are rewritten in a central difference scheme, with $N_x \times N_{c_x}$ grid points distributed uniformly along $x \in [-0.5, 0.5]$ and non-uniformly along $c_x \in (-\infty, \infty)$ directions. A coupled set of $2N_xN_{c_x}$ non-homogeneous algebraic equations for $\bar{\psi}_{1_b}$ and $\bar{\psi}_2$, together with $3N_x$ equations defining $\bar{\rho}$, $\bar{u}$, and $\bar{T}$, collate into a sparse system of equations. Our calculations indicate that, to achieve a converged result within a 1% error, a choice of $N_x = N_{c_x} = 256$ grid points is sufficient. For a given combination of Kn and ω, the system of equations was solved efficiently in a few minutes run on a standard laptop machine.

Once wall motion actuations $U_{w_\pm}(t)$ are prescribed, the frequency-domain solution is obtained for each component contained in $\bar{U}_{w_\pm}(\omega)$. After calculation of all Fourier components, the time-domain solution is computed via an inverse Fourier transform,

$$Q(t) = \frac{1}{2\pi}\int_{-\infty}^{\infty} \bar{Q}(\omega)\exp\left[\mathrm{i}\omega t\right]\mathrm{d}\omega. \tag{50}$$

In cases where the Fourier spectrum of the signal is infinite (as in the case analyzed in Sec. V), the spectrum is discretized and truncated to enable numerical solution. Accuracy of results is validated in Sec. V through comparison with other methods of solution.

C. Continuum limit

While the solution in the continuum limit of $Kn \ll 1$ can be obtained by application of the general scheme in Sec. III B at low Knudsen numbers, we make use of a continuum-limit model, based on the continuum (Navier-Stokes-Fourier) equations and modified ("slip-flow") boundary conditions, to obtain independent results. In addition to deriving semi-analytical predictions, comparison of the continuum-limit analysis with the general numerical solution will serve to test the limits of validity of the continuum description in the present problem.

Starting with the full set of normalized continuum equations (non-dimensionalized using the scales introduced in the beginning of Sec. II), and linearizing about the initial equilibrium state, we obtain the balances of mass, momentum and energy for the $O(\varepsilon)$ density, normal velocity, and temperature perturbations,

$$\frac{\partial \rho}{\partial t} + \frac{\partial u}{\partial x} = 0\,, \tag{51}$$

$$\frac{\partial u}{\partial t} = -\frac{1}{2}\left(\frac{\partial \rho}{\partial x} + \frac{\partial T}{\partial x}\right) + \frac{4\widetilde{Kn}}{3}\frac{\partial^2 u}{\partial x^2}\,, \tag{52}$$

and

$$\frac{\partial T}{\partial t} = \frac{\gamma \widetilde{Kn}}{Pr}\frac{\partial^2 T}{\partial x^2} - (\gamma - 1)\frac{\partial u}{\partial x}\,. \tag{53}$$

Here $\widetilde{Kn} = \nu^*/U_{th}^* L^*$ is the modified Knudsen number with ν^* denoting the mean kinematic viscosity of the gas. The modified Knudsen number is related to Kn through

$$\widetilde{Kn} = \frac{\nu^*}{U_{th}^* l^*} Kn, \tag{54}$$

where $\nu^*/U_{th}^* l^* = \sqrt{\pi}/4$ for a BGK gas.[22] In (53), γ and Pr mark the ratio of specific heats and Prandtl number, respectively, with $\gamma = 5/3$ and $Pr = 1$ for a BGK gas. Equations (51)–(53) are supplemented by the boundary conditions

$$u = U_{w_\pm}(t) \text{ and } T = \pm\xi\frac{\partial T}{\partial x} \text{ at } x = \mp 1/2, \tag{55}$$

imposing impermeability and specifying the magnitude of temperature jump at the walls. The latter is determined by the value of temperature gradient at the boundaries and a temperature-jump coefficient, $\xi = \zeta Kn$, where $\zeta = 1.3\sqrt{\pi}/2$ for a BGK gas.[22]

Similarly to the analysis carried out in Sec. III B, we apply the Fourier transform (27) to Eqs. (51)–(55). This yields a system of ordinary equations

$$\mathrm{i}\omega\bar{\rho} + \bar{u}' = 0, \tag{56}$$

$$\mathrm{i}\omega\bar{u} = -\frac{1}{2}\left(\bar{\rho}' + \bar{T}'\right) + \frac{4\widetilde{Kn}}{3}\bar{u}'', \tag{57}$$

$$\mathrm{i}\omega\bar{T} = \frac{5\widetilde{Kn}}{3}\bar{T}'' - \frac{2}{3}\bar{u}', \tag{58}$$

accompanied by the boundary conditions

$$\bar{u} = \bar{U}_{w_\pm}(\omega) \text{ and } \bar{T} = \pm\xi\bar{T}' \text{ at } x = \mp 1/2, \tag{59}$$

where primes denote differentiations with x. The density and velocity perturbations can be eliminated using

$$\bar{\rho} = \frac{\mathrm{i}}{\omega}\bar{u}'\,,\quad \bar{u} = -\frac{5\widetilde{Kn}}{2\omega}\left(\frac{1}{2\omega} + \frac{4\mathrm{i}\widetilde{Kn}}{3}\right)\bar{T}''' - \left(2\widetilde{Kn} - \frac{5\mathrm{i}}{4\omega}\right)\bar{T}' \tag{60}$$

to yield a single equation for the temperature,

$$\frac{5\widetilde{Kn}}{3}\left(\frac{4\widetilde{Kn}}{3} - \frac{\mathrm{i}}{2\omega}\right)\bar{T}'''' - \left(3\mathrm{i}\omega\widetilde{Kn} + \frac{5}{6}\right)\bar{T}'' - \omega^2\bar{T} = 0, \tag{61}$$

which should be solved in conjunction with the four boundary conditions

$$-\frac{5\widetilde{Kn}}{2\omega}\left(\frac{1}{2\omega} + \frac{4\mathrm{i}\widetilde{Kn}}{3}\right)\bar{T}''' - \left(2\widetilde{Kn} - \frac{5\mathrm{i}}{4\omega}\right)\bar{T}' = \bar{U}_\pm(\omega) \quad \text{and}$$
$$\bar{T} = \pm\xi\bar{T}' \text{ at } x = \mp 1/2\,. \tag{62}$$

The characteristic polynomial of Eq. (61) has four distinct roots:

$$r_{1,2}(\omega) = \pm\left[\frac{-a_1 + \sqrt{a_1^2 - 4a_2a_0}}{2a_2}\right]^{1/2} \quad \text{and} \quad r_{3,4}(\omega) = \pm\left[\frac{-a_1 - \sqrt{a_1^2 - 4a_2a_0}}{2a_2}\right]^{1/2}, \tag{63}$$

where a_0, a_1, and a_2 are the coefficients multiplying $\bar{T}$, $\bar{T}''$, and $\bar{T}''''$ in (61), respectively. The solution for the temperature perturbation is given by

$$\bar{T}(x,\omega) = \sum_{k=1}^{4} C_k(\omega)\exp\left[r_k(\omega)x\right], \tag{64}$$

where the constants of integration C_k are determined by the boundary conditions (62). Expressions for the Fourier-transformed density and velocity perturbations now follow from substitution of Eq. (64) into Eq. (60). The time-domain solution is obtained by taking the real part of the inverse Fourier transform (50) of each of the transformed hydrodynamic fields.

IV. LVDSMC SCHEME

The methods described in Sec. III were validated using the low-variance deviational simulation Monte Carlo (LVDSMC) method,[23] which is able to capture near equilibrium flows at a greatly reduced computational cost compared to the standard direct simulation Monte Carlo (DSMC) method,[24] and without introducing approximations. The original LVDSMC method was developed for hard-sphere collisions,[25] but variants exist for both BGK[26–28] and variable hard sphere[28,29] collisions. In this work, we make use of a recent mass-conservative version which features zero time step error in the collision step; the BGK version with these features is documented in Ref. 28. The mass-conservative formulation[28,29] eliminates random walks in the hydrodynamic variables without a need for large numbers of computational particles, as was required by earlier methods. Below is a brief outline of the computational method and a description of how it was extended to treat moving boundaries.

The LVDSMC method presented here solves the BGK model equation by decomposing the velocity distribution $f = f^0 + f^d$ into a reference equilibrium, here taken to be $f^0 = F$, and a deviation from equilibrium f^d simulated by signed particles, representing positive and negative deviations from the reference state. The resulting equation for f^d (assuming one-dimensional flow and zero body forces) is

$$\frac{\partial f^d}{\partial t} + c_x\frac{\partial f^d}{\partial x} = \frac{2}{\sqrt{\pi}Kn}\left(f^{loc} - f^0\right) - \frac{2f^d}{\sqrt{\pi}Kn}, \tag{65}$$

where f^{loc} is the local equilibrium (Maxwell-Boltzmann) distribution based on local hydrodynamic properties. Note that the advection part in Eq. (65) is identical with the original Boltzmann equation, and thus deviational particles are advected along velocity trajectories as in the standard DSMC procedure. The collision part is simulated by creating new deviational particles through sampling the distribution $2\left(f^{loc} - f^0\right)/\left(\sqrt{\pi}Kn\right)$ and deleting existing particles from f^d; this deletion step is the key to providing stability of the method by countering an unbounded increase in the number of particles in simulation.

Enforcement of the moving boundary condition is accomplished in two steps, the first of which is the standard LVDSMC technique[28,29] simplified for diffuse reflections. At the boundaries $x = \mp 1/2$, the distribution function for $c_x \gtrless \varepsilon U_{w_\pm}$ is

$$f^d = \rho_B^{refl}\phi^B + \left(\rho_B^{gen}\phi^B - f^0\right), \tag{66}$$

where $\phi^B = \pi^{-3/2}\exp\left(-(c_x - \varepsilon U_{w_\pm})^2 + c_y^2 + c_z^2\right)$. The first term in Eq. (66) represents particles which strike the boundary and reflect diffusely, in a standard DSMC procedure, where the velocity of the particle is sampled from the fluxal boundary distribution $\pm(c_x - \varepsilon U_{w_\pm})\phi^B$, which maintains the initial sign of the particle. Implementing the second term in Eq. (66) requires sampling deviational

particles from the distribution $\pm(c_x - \varepsilon U_{w_\pm})\left(\rho_B^{gen}\phi^B - f^0\right)$, where ρ_B^{gen} is determined from mass conservation,

$$\rho_B^{gen} = -\frac{\int_{c_x \lessgtr \varepsilon U_{w_\pm}} (c_x - \varepsilon U_{w_\pm}) f^0 \mathrm{d}^3\mathbf{c}}{\int_{c_x \gtrless \varepsilon U_{w_\pm}} (c_x - \varepsilon U_{w_\pm}) \phi^B \mathrm{d}^3\mathbf{c}} \,. \tag{67}$$

A second step is required in the enforcement of the deviational boundary condition during the wall movement. For a time step δt the domain contracts (expands) by $\varepsilon\left(U_{w_+} - U_{w_-}\right)\delta t$, resulting in removal (addition) of the underlying equilibrium state f^0 in the region. To correct for this, and to restore the correct reference state in the region, additional particles are introduced at the boundary via the fluxal distribution $\varepsilon U_{w_\pm}\delta t(c_x - U_{w_\pm})\phi^B$, where we have used the fact that the dimensionless reference distribution has unit density. Explicit mass conservation for this step is enforced by tracking a mass residual at each boundary, defined as the sum of the differences between the mass of generated particles and the exact mass changes $\pm\varepsilon U_{w_\pm}\delta t$, for all time steps up to the current time. The number of generated particles is chosen to minimize the absolute value of the residual at each boundary, ensuring that the mass is conserved to nearest integer particle count. Mass conservation for all other steps is enforced using established procedures described in Refs. 28 and 29.

Hydrodynamic properties are evaluated by summing appropriate moments of the deviation particles in each cell and normalizing by the volume. Since the absolute movements of boundary surfaces were small, only the cells adjacent to the boundaries were dynamically resized, rather than requiring a dynamic remesh of the entire domain.

V. RESULTS

While the analysis described in Secs. III and IV can be applied to any small-amplitude motion of the boundaries, we focus here on a particular case of "bump-like" actuation,

$$U_{w_\pm}(t) = \begin{cases} \pm 1, & 0 \le t \le t_b \\ 0, & \text{otherwise} \end{cases} \,, \tag{68}$$

in which t_b governs the bump duration and is taken $t_b = 0.1$ (in acoustic-time units, L^*/U_{th}^*). By choosing the profile (68), we aim at analyzing the gas response to instantaneous (short-time) non-periodic forcing, in which both boundaries act as sound generators. The mirror-like motion of the boundaries facilitates numerical calculation by requiring solution for only half of the gas domain (and then applying symmetry properties to obtain the system behavior at the other half of the channel). This is particularly useful for carrying out LVDSMC calculations, which become computationally expensive for simulating flows at low Knudsen numbers. In the following, we compare our analytical results in the ballistic and continuum limits with numerical solutions based on the linearized BGK equation and LVDSMC scheme.

Figures 1 and 2 present time variations of the density, velocity, temperature, and pressure perturbations for $Kn = 5$ (Fig. 1) and $Kn = 0.02$ (Fig. 2) at fixed locations ($x = -0.4$ and $x = -0.2$) along the gap. Each figure shows comparison between the analytical approximation (being the ballistic-limit solution in Fig. 1 and the continuum-limit solution in Fig. 2) and numerical LVDSMC (crosses) and linearized BGK (circles) solutions. In general, the agreement between all sets of results is very good at almost all times, supporting use of each of the independent schemes at the chosen Knudsen numbers. Given the vastly different methods of solution applied, we find this agreement gratifying.

Starting with the large-Kn case (Fig. 1), we observe that at early times there exists an initial time interval, Δt_r, during which all perturbations equal zero. This "retarded time" interval reflects the time it takes the moving-wall signal to reach the point in space where perturbations are measured. Naturally, Δt_r is larger for $x = -0.2$ than for $x = -0.4$, as the former is located further away from the walls. Recalling that the time is scaled by the acoustic time scale L^*/U_{th}^*, and focusing on the instant in time when the wavefront first reaches the measurement point, we find that the disturbance initially propagates from the wall at the mean thermal speed.[30] A similar result was found for the

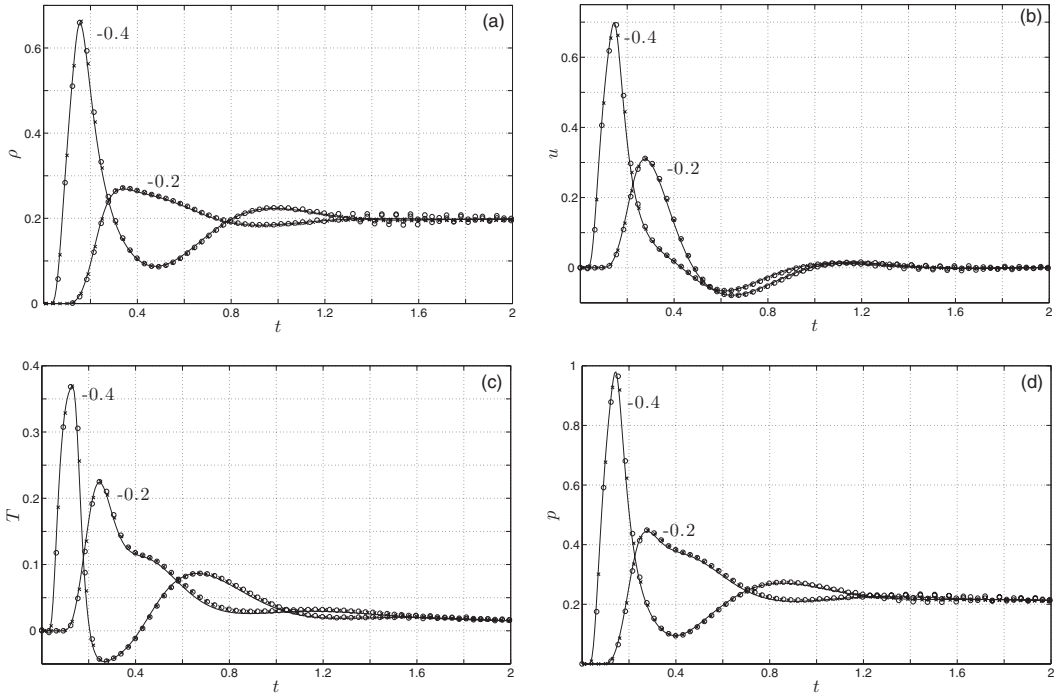

FIG. 1. Time variations of (a) density, (b) velocity, (c) temperature, and (d) pressure perturbations for $Kn = 5$ and the indicated fixed locations $x = -0.4$ and $x = -0.2$ along the gap. Solid lines, crosses, and circles denote analytical (collisionless), LVDSMC, and linearized BGK solutions, respectively.

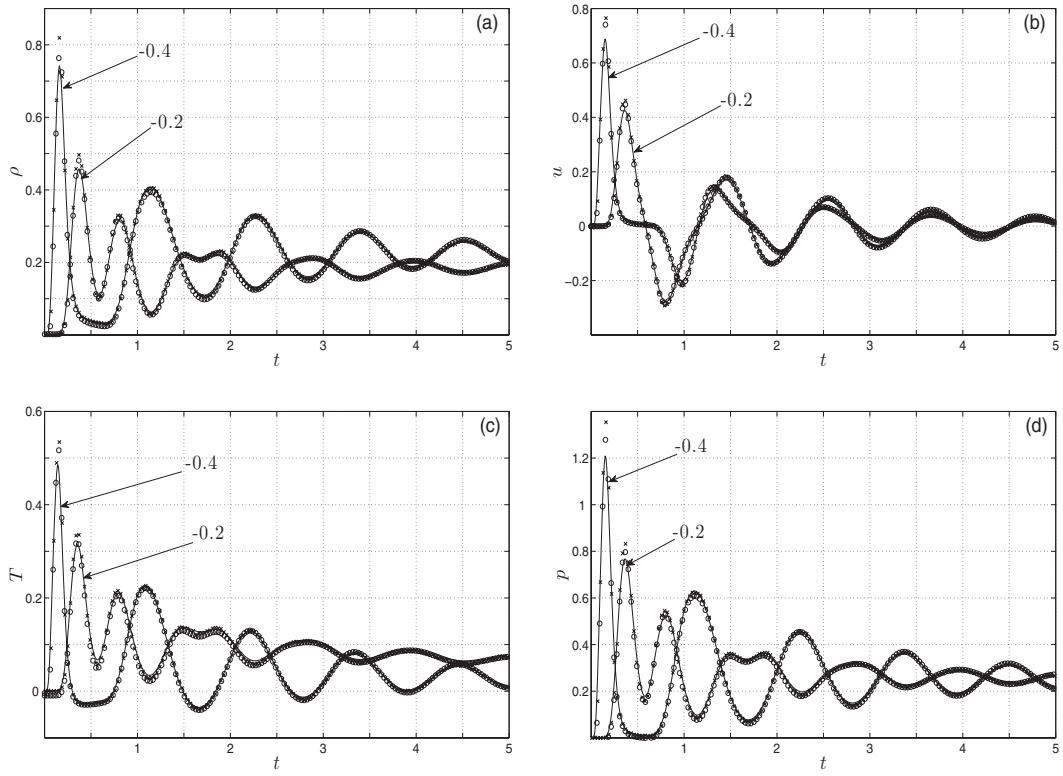

FIG. 2. Time variations of (a) density, (b) velocity, (c) temperature, and (d) pressure perturbations for $Kn = 0.02$ and the indicated fixed locations $x = -0.4$ and $x = -0.2$ along the gap. Solid lines, crosses and circles denote analytical (continuum-limit), LVDSMC, and linearized BGK solutions, respectively.

gas response to instantaneous boundary heating.[31] Generally, the motion of each boundary at early times ($t \ll 1$) affects only its immediate vicinity, and the total system behavior can be viewed as a superposition of the local gas responses to two walls interacting with a semi-infinite medium.

As the signal wavefront passes a point in space, all hydrodynamic perturbations exhibit a local sharp increase in their magnitudes, followed by a later decrease. While density and pressure perturbations remain positive at all times, it is interesting to note that the temperature perturbation becomes negative close to the boundary after first passage of the wavefront (see the curve pertaining to $x = -0.4$ in Fig. 1(c) for $0.2 \lesssim t \lesssim 0.5$). With increasing time, the mutual effects of both walls are reflected at each point in the gas domain. Thus, the minima of negative velocities observed in Fig. 1 b at $t \approx 0.6$ originate from the motion of the wall at $x = 0.5$ in the negative-x direction. At later times, the gas approaches its new equilibrium state through a series of decaying waves propagating across the gap. For the present case of two isothermal walls displaced a t_b-distance into the gas domain (in εL^* units) after the bump, the new equilibrium state is given by uniformly vanishing temperature and velocity perturbations, together with steady-state density and pressure perturbations given by

$$\rho(t \to \infty) \approx p(t \to \infty) \approx 2t_b. \tag{69}$$

These steady-state values, resulting from the reduction in channel width from L^* to $L^*(1 - 2t_b\varepsilon)$ owing to walls motion, are clearly recovered in the late-time behavior in Fig. 1. Remarkably, the new equilibrium state is achieved shortly after $t \approx 1$, which corresponds to approximately one-fifth of the mean free time for the present choice of $Kn = 5$. Given the short relaxation process, it is indeed expected that the collisionless analysis should predict the exact numerical solution well. To this end, the small-amplitude rapid oscillations visible in the linearized BGK solution at late times, reflect only numerical discretization of the inverse Fourier transform calculation, and vanish with increasing the number and range of frequency components included in the integration.

Traversing to the low-Kn case presented in Fig. 2, we observe several qualitative differences between the system behavior at collisionless and continuum-limit conditions. Perhaps the most visible difference is in the oscillatory behavior of the system at small Kn, being much weaker at high-Kn flow conditions. This is accompanied by extension in equilibration time with decreasing Kn, being $t \gtrsim 10$ (outside the time interval presented in the figure) for $Kn = 0.02$. Oscillations period approximately equals unity, reflecting the time it takes for a disturbance to propagate across the gap (see discussion of Fig. 1). With increasing t, oscillations amplitude decays owing to viscous dissipation effects. Similarly to Fig. 1, negative values of the temperature perturbation are observed at early times close to the wall, after passage of first and second wavefronts.

Comparing between the responses presented in Figs. 1 and 2, it appears that the Knudsen number, governing the amount of collisions experienced by a molecule while passing through the channel, can be viewed in the present context as a "damping coefficient": at large values, when molecular collisions are infrequent, equilibration is achieved almost instantaneously at times $O(L^*/U_{th}^*)$, much shorter than the mean free time ($\sim l^*/U_{th}^*$); however, when $Kn \ll 1$, equilibration is obtained through extended oscillations, captured well by the continuum-limit solution. With decreasing Kn, equilibration becomes more and more affected by the diffusive time scale L^{*2}/ν^*, being $1/Kn$ longer than the acoustic scale (see Eq. (54)). Note that, while the analytical solution is in close agreement with simulations at almost all times, significant discrepancies appear in Fig. 2 at $t < 1$, particularly when perturbation wavefront passes through the measurement point (observe the differences between results at the first maximum point in all fields in Fig. 2). Indeed, all hydrodynamic fields exhibit sharp time-variations in the vicinity of perturbation wavefront, resulting in a local decrease in the characteristic time-scale and subsequent increase in the equivalent value of *local* Knudsen number (see Fig. 3). These discrepancies diminish in time, when the wavefront flattens due to viscous dissipation effects. At early times, small differences are also observed in Fig. 2 between linearized BGK and LVDSMC results, and are attributed mainly to a small inevitable inaccuracy in LVDSMC data due to numerical discretization. A more refined LVDSMC calculation would become considerably demanding for the present small value of Kn. In terms of validity of our analytical scheme, our calculations indicate that the differences between continuum-limit and exact (LVDSMC and linearized BGK) solutions vanish with decreasing Kn.

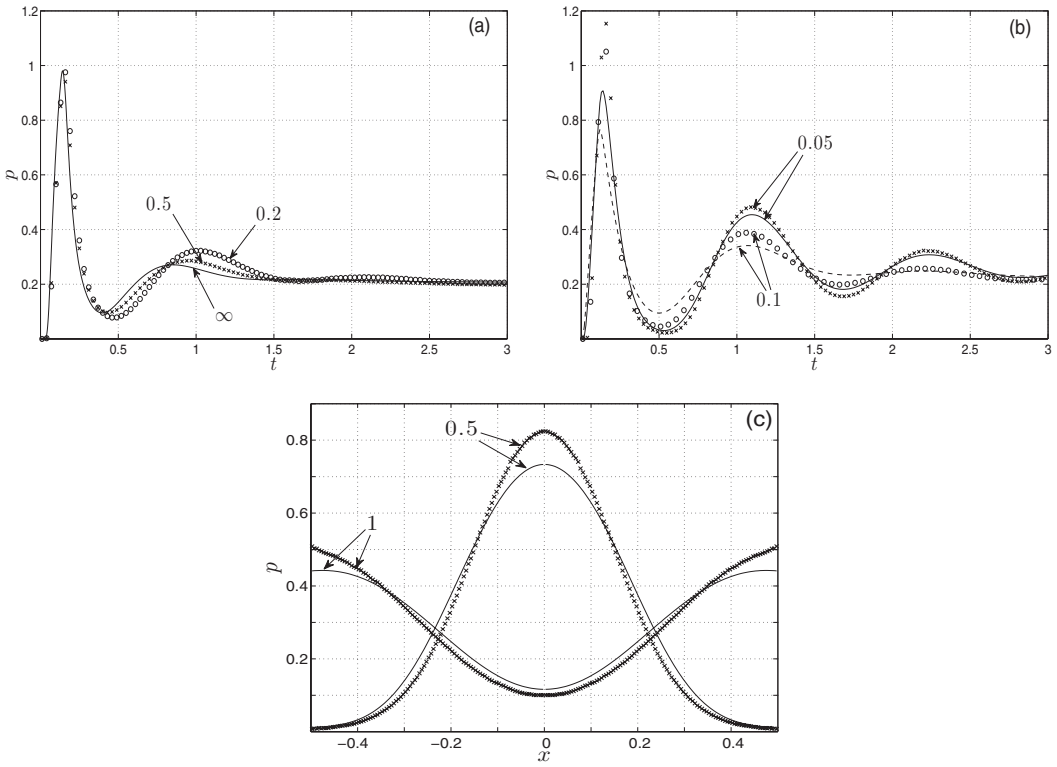

FIG. 3. Effect of the Knudsen number on the variation of pressure perturbation: (a) comparison between time evolution in the ballistic limit ($Kn \to \infty$, solid line) and LVDSMC results for $Kn = 0.5$ (crosses) and $Kn = 0.2$ (circles) at $x = -0.4$; (b) comparison between time evolution calculated using continuum-limit analysis (dashed and solid lines) and LVDSMC scheme (circles and crosses) for $Kn = 0.1$ and $Kn = 0.05$, respectively, at $x = -0.4$; and (c) time snapshots of pressure perturbation at the indicated times, for $Kn = 0.05$. Solid lines and crosses mark continuum-limit and LVDSMC data, respectively.

To examine the limits of validity of the analytical approximations, Figure 3 studies the effect of the Knudsen number on the time and space variations of the pressure perturbation. Figures 3(a) and 3(b) study the time evolution of pressure at a fixed point ($x = -0.4$), whereas Fig. 3(c) presents the pressure space variation. Specifically, Fig. 3(a) compares the collisionless solution with LVDSMC results for $Kn = 0.5$ and $Kn = 0.2$, and Fig. 3(b) compares the continuum-limit predictions with LVDSMC data for $Kn = 0.05$ and $Kn = 0.1$. Figure 3(c) studies the case $Kn = 0.05$ and compares the calculated space variation according to LVDSMC and continuum-limit schemes at times $t = 0.5$ and $t = 1$.

Starting with Fig. 3(a), we observe that the collisionless solution approximates the numerical result reasonably well for $Kn = 0.5$, and, to a qualitative degree, even for $Kn = 0.2$. Yet, quantitative discrepancies are clearly detected in both cases, resulting from the effect of molecular collisions, which becomes non-negligible for $Kn < 1$ at $t \gtrsim O(1)$. Turning to Fig. 3(b), we find that the differences between continuum-limit and exact numerical solutions increase with increasing Kn. As noted in Fig. 2, these differences are most significant close to the maxima points, marking the times when perturbation wavefront passes through the measurement location $x = -0.4$. For $Kn = 0.1$, these discrepancies become of the order of 10% and more. It can therefore be concluded that, while the collisionless solution predicts the system behavior markedly well up to $Kn \approx 1$ and somewhat less, more care should be taken when applying the continuum-limit description to analyze the system behavior in the vicinity of perturbation wavefront.

To further illustrate the last observation, the space variations of pressure perturbation presented in Fig. 3(c) show that the maximum discrepancies between approximate (continuum-limit) and numerical solutions appear at wavefront locations. Recalling that the wavefront propagates at the mean thermal speed, it is located at the middle of the gap $x \approx 0$ when $t = 0.5$, and at $x \approx \pm 0.5$ (close

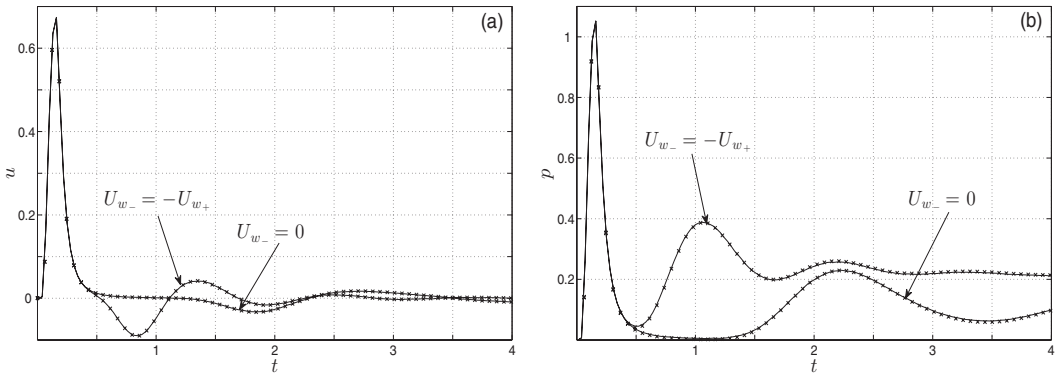

FIG. 4. Effect of two-walls motion on the time evolution of (a) velocity and (b) pressure perturbations for $Kn = 0.1$ at $x = -0.4$. Each figure shows time variations in cases of antisymmetric motion of the walls ($U_{w_-} = -U_{w_+}$), and when the wall at $x = 0.5$ is stationary ($U_{w_-} = 0$). Solid lines and crosses mark LVDSMC and linearized BGK data, respectively.

to the boundaries) when $t = 1$. Indeed, the largest discrepancies are observed at these locations in the respective curves. Given this cause for breakdown of the continuum description, it is yet satisfactory that the continuum-limit approximation provides a reasonable prediction for the overall system behavior at non-vanishing Knudsen numbers.

To complete the presentation of results, Figure 4 studies the effect of having two moving walls (as prescribed in Eq. (68)), by comparing the present results for velocity (Fig. 4(a)) and pressure (Fig. 4(b)) perturbations at $x = -0.4$, with those obtained when having only one moving wall,

$$U_{w_+}(t) = \begin{cases} 1\,, & 0 \le t \le t_b \\ 0\,, & \text{otherwise} \end{cases}, \quad U_{w_-}(t) \equiv 0, \tag{70}$$

with $t_b = 0.1$. The two setups are compared for $Kn = 0.1$, and for each case, both LVDSMC and linearized BGK results are presented. Again we note that the numerical solutions are in very good agreement, in support of their accuracy.

At early times ($t \lesssim 0.5$), we observe that the two solutions are identical. Indeed, the only signal affecting the gas at $x = -0.4$ at these times, is the one generated by the moving wall at $x = -0.5$, common to both setups. The effect of distant wall actuation becomes significant at later times, where the two solutions differ, reflecting pressure wave propagation from $x = 0.5$ in the two-moving-wall case (see the non-monotonic variation for $U_{w_-} = -U_{w_+}$ at $0.5 \lesssim t \lesssim 1.5$ in both Figs. 4(a) and 4(b)). At late times, the two systems approach different equilibrium states, as the steady state pressure for the $U_{w_-} = 0$ system is $p(t \to \infty) \approx t_b = 0.1$ (cf. Eq. (69)). Equilibration time was found similar in both cases.

VI. CONCLUSION

We studied the response of a gas in a microchannel to instantaneous non-periodic small-amplitude boundary motion in the normal direction. The problem was formulated using the BGK model,[20] and solved for the entire range of Knudsen numbers, combining analytical and numerical schemes of solution. System response to short time (compared to the ballistic time scale L^*/U^*_{th}) "bump-like" boundary actuation was analyzed, showing a sequence of propagating and reflected pressure waves, decaying in time towards an equilibrium state achieved at late times. Gas rarefaction was found to have a damping effect on the relaxation process, with the time required for equilibrium shortening with increasing Kn. Oscillations in hydrodynamic quantities, characterizing gas response in continuum-limit conditions, were shown to vanish in the collisionless limit. The effect of having two moving boundaries, compared to only one considered in previous studies, was investigated, demonstrating the added effect of having two sources of sound in the system. Comparison between analytical and numerical solutions revealed that the collisionless description predicts the system

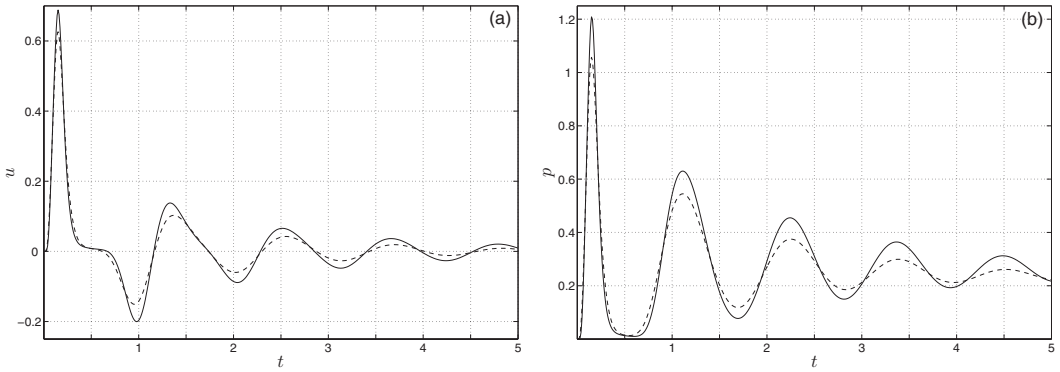

FIG. 5. Comparison between BGK (solid lines) and hard-sphere gas (dashed lines) model predictions for the time variations of (a) velocity and (b) pressure perturbations at $x = -0.4$ and $Kn = 0.02$. Results are based on continuum-limit scheme in Sec. III C.

behavior exceptionally well for all $Kn \gtrsim 1$ and somewhat less. Yet, the continuum-limit solution should be considered with care at early times near the location of acoustic wavefronts, where the local scale characterizing flow-field variations becomes small and increases the effective value of local Knudsen number. In spite of this limitation, and recalling the relative effort required in obtaining numerical results, the analytical approximations are suggested as an efficient alternative for predicting the overall system behavior. Practically, to obtain exact quantitative description of the system response to short-time excitation, numerical solution is needed only at a narrow interval of $0.1 \lesssim Kn \lesssim 0.5$ numbers, where collisionless and continuum-limit schemes break down (see Fig. 3). In cases where boundary motion extends over longer periods of time (of the order of the ballistic time scale and longer), the collisionless solution is expected to hold only at short times ($t^* \lesssim L^*/U^*_{th}$) for systems with $Kn \sim O(1)$, while numerical solution will be needed to capture later-time system evolution.

The analysis presented in this work is based on the BGK model of the Boltzmann equation. The same model equation was adopted in previous studies on acoustic wave propagation (e.g., Refs. 4, 8, 9, 13, and 19), mainly owing to its relative simplicity, which facilitates derivation of semi-analytical and numerical solutions. Yet, a well known deficiency of the model is that it does not predict the correct value for the Prandtl number for a monatomic gas (unity instead of 2/3), and therefore cannot yield the accurate coupling between gas dynamic and thermodynamic descriptions. While this is generally true, we note that a key part of our analysis focuses on a collisionless-flow problem, which formulation is independent of the chosen model of molecular interaction. In addition, and as mentioned above, our findings indicate that when the input signal acts during a time interval that is shorter than the ballistic time-scale, the collisionless-flow limit predicts the entire system behavior remarkably well for Knudsen numbers as low as unity and somewhat smaller. This indicates that the role of chosen model of molecular interaction in the present problem is not dominant for a wide range of gas-rarefaction conditions.

To further investigate on the effect of chosen model of molecular interaction, Figure 5 presents a comparison between the responses of BGK and hard-sphere gases to "bump-like" actuation, as obtained using the continuum-limit scheme (see Sec. III C). The time variations of velocity and pressure perturbations are presented at a fixed point ($x = -0.4$), for a system with $Kn = 0.02$. Hard-sphere data are obtained by replacing the BGK entries in the model of Sec. III C by their hard-sphere counterparts, $Pr = 2/3$, $\widetilde{Kn} \approx 0.225Kn$ and $\xi \approx 2.127Kn$, respectively.[22] As clearly observed in both parts of the figure, only minor (qualitatively insignificant) differences appear between the results. This supports the present application of the BGK model, as it is expected that the effect of molecular interaction should be most dominant at small Knudsen numbers, where molecular collisions are frequent. A similar conclusion can be drawn by carrying out a numerical solution based on the LVDSMC scheme, readily available for a hard-sphere gas[25] and other models of molecular interaction.[29] Regardless of the chosen model of molecular interaction, the main contribution of

the present work is in presenting a general scheme for studying propagation of acoustic waves in a confined domain, resulting from *arbitrary* (small-amplitude) boundary actuation. This is in contrast with existing studies (excluding Ref. 19), which have hitherto considered system response to harmonic actuation only.

Focusing on a case of non-periodic excitation, the present study quantifies the damping effect of gas rarefaction on sound-wave propagation in a confined geometry. We find that while the relaxation time at collisionless-flow conditions is $\sim O(L^*/U_{th}^*)$, equilibration process extends over longer times with decreasing Kn (cf. Figs. 1 and 2). This can be traced back to the ratio between advective ($\sim L^*/U_{th}^*$) and diffusive ($\sim L^{*2}/\nu^*$) time scales, governing relaxation processes in collisionless and continuum conditions, respectively. A similar result was found in a previous set of studies, where the thermoacoustic response of a gas to instantaneous (step-jump) change in the temperature of its boundaries was analyzed.[31,32] It therefore appears of interest to investigate the combined effects of thermal and mechanical excitations on the propagation of sound waves in a rarefied medium.[33] Extension of the present theory to spatially two- and three-dimensional configurations may also be considered, but will be based mainly on demanding numerical simulations, which are not in the focus of the present contribution.

APPENDIX: DERIVATION OF EQS. (15) AND (16)

Substituting Eq. (13) into Eq. (14), and carrying out the c_y and c_z integrations, yield

$$\rho_+(t) + 2\int_{-\infty}^{-1/t} \rho_-\left(t + 1/c_x\right) c_x \exp\left[-c_x^2\right] \mathrm{d}c_x = \sqrt{\pi} U_{w_+}(t) - 4\int_{-\infty}^{-1/t} U_{w_-}\left(t + 1/c_x\right) c_x^2 \exp\left[-c_x^2\right] \mathrm{d}c_x \tag{A1}$$

and

$$\rho_-(t) - 2\int_{1/t}^{\infty} \rho_+\left(t - 1/c_x\right) c_x \exp\left[-c_x^2\right] \mathrm{d}c_x = -\sqrt{\pi} U_{w_-}(t) + 4\int_{1/t}^{\infty} U_{w_+}\left(t - 1/c_x\right) c_x^2 \exp\left[-c_x^2\right] \mathrm{d}c_x. \tag{A2}$$

Changing the variables in the integral terms in (A1) and (A2) to $\tau = t + 1/c_x$ and $\tau = 1 - 1/c_x$, respectively, leads to

$$\rho_+(t) - 2\int_0^t \frac{\rho_-(\tau)}{(t-\tau)^3} \exp\left[-\frac{1}{(t-\tau)^2}\right] d\tau = \sqrt{\pi} U_{w_+}(t) - 4\int_0^t \frac{U_{w_-}(\tau)}{(t-\tau)^4} \exp\left[-\frac{1}{(t-\tau)^2}\right] d\tau \tag{A3}$$

and

$$\rho_-(t) - 2\int_0^t \frac{\rho_+(\tau)}{(t-\tau)^3} \exp\left[-\frac{1}{(t-\tau)^2}\right] d\tau = -\sqrt{\pi} U_{w_-}(t) + 4\int_0^t \frac{U_{w_+}(\tau)}{(t-\tau)^4} \exp\left[-\frac{1}{(t-\tau)^2}\right] d\tau. \tag{A4}$$

Integration by parts of the integral terms on the left-hand sides of Eqs. (A3) and (A4) yields Eqs. (15) and (16), respectively.

[1] J. Lighthill, *Waves in Fluids* (Cambridge University Press, New York, 1978).
[2] M. Greenspan, "Propagation of sound in five monatomic gases," J. Acoust. Soc. Am. **28**, 644–648 (1956).
[3] E. Meyer and G. Sessler, "Schallausbreitung in Gasen bei hohen Frequenzen und sehr niedrigen Drucken," Z. Phys. **149**, 15–29 (1957).
[4] L. Sirovich and J. K. Thurber, "Propagation of forced sound waves in rarefied gas dynamics," J. Acoust. Soc. Am. **37**, 329–339 (1965).
[5] G. Maidanik, H. L. Fox, and M. Heckl, "Propagation and reflection of sound in rarefied gases. I. Theoretical," Phys. Fluids **8**, 259–265 (1965).

[6] G. Maidanik and M. Heckl, "Propagation and reflection of sound in rarefied gases. II. Experimental," Phys. Fluids **8**, 266–272 (1965).
[7] J. Foch and G. E. Uhlenbeck, "Propagation of sound in monatomic gases," Phys. Rev. Lett. **19**, 1025–1027 (1967).
[8] S. K. Loyalka and T. C. Cheng, "Sound-wave propagation in a rarefied gas," Phys. Fluids. **22**, 830–836 (1979).
[9] J. R. Thomas, Jr. and C. E. Siewert, "Sound-wave propagation in a rarefied gas," Transport Theory Stat. **8**, 219–240 (1979).
[10] N. G. Hadjiconstantinou, "Sound wave propagation in transition-regime micro- and nanochannels," Phys. Fluids. **14**, 802–809 (2002).
[11] F. Sharipov, W. Marques, Jr., and G. M. Kremer, "Free molecular sound propagation," J. Acoust. Soc. Am. **112**, 395–401 (2002).
[12] N. G. Hadjiconstantinou and O. Simek, "Sound propagation at small scales under continuum and non-continuum transport," J. Fluid Mech. **488**, 399–408 (2003).
[13] R. D. M. Garcia and C. E. Siewert, "The linearized Boltzmann equation: Sound-wave propagation in a rarefied gas," Z. Angew. Math. Phys. **57**, 94–122 (2005).
[14] F. Sharipov and D. Kalempa, "Numerical modeling of the sound propagation through a rarefied gas in a semi-infinite space on the basis of linearized kinetic equation," J. Acoust. Soc. Am. **124**, 1993–2001 (2008).
[15] D. Kalempa and F. Sharipov, "Sound propagation through a rarefied gas confined between source and receptor at arbitrary Knudsen number and sound frequency," Phys. Fluids **21**, 103601 (2009).
[16] L. Desvillettes and S. Lorenzani, "Sound wave resonances in micro-electro-mechanical systems devices vibrating at high frequencies according to the kinetic theory of gases," Phys. Fluids **24**, 092001 (2012).
[17] H. Struchtrup, "Resonance in rarefied gases," Continuum Mech. Thermodyn. **24**, 361–376 (2012).
[18] A. L. Danforth and L. N. Long, "Nonlinear acoustic simulations using direct simulation Monte Carlo," J. Acoust. Soc. Am. **116**, 1948–1955 (2004).
[19] T. Tsuji and K. Aoki, "Moving boundary problems for a rarefied gas: Spatially one-dimensional case," J. Comput. Phys. **250**, 574–600 (2013).
[20] P. L. Bhatnagar, E. P. Gross, and M. Krook, "A model for collisional processes in gases. I: Small amplitude processes in charged and in neutral one-component systems," Phys. Rev. **94**, 511–525 (1954).
[21] M. N. Kogan, *Rarefied Gas Dynamics* (Plenum, New York, 1969).
[22] Y. Sone, *Molecular Gas Dynamics: Theory, Techniques, and Applications* (Birkhäuser, Boston, 2007).
[23] G. A. Radtke, J.-P. M. Peraud, and N. G. Hadjiconstantinou, "On efficient simulations of multiscale kinetic transport," Philos. Trans. R. Soc. A **371**, 2012182 (2013).
[24] G. Bird, *Molecular Gas Dynamics and the Direct Simulations of Gas Flows* (Clarendon, Oxford, 1994).
[25] T. M. M. Homolle and N. G. Hadjiconstantinou, "A low-variance deviational simulation monte carlo for the Boltzmann equation," J. Comput. Phys. **226**, 2341–2358 (2007).
[26] G. A. Radtke and N. G. Hadjiconstantinou, "Variance-reduced particle simulation of the Boltzmann transport equation in the relaxation-time approximation," Phys. Rev. E **79**, 056711 (2009).
[27] N. G. Hadjiconstantinou, G. A. Radtke, and L. L. Baker, "On variance-reduced simulations of the Boltzmann transport equation for small-scale heat transfer applications," J. Heat Transfer **132**, 112401 (2010).
[28] G. A. Radtke, "Efficient simulation of molecular gas transport for micro- and nanoscale applications," Ph.D. thesis (Massachusetts Institute of Technology, Cambridge, MA, 2011).
[29] G. A. Radtke, N. G. Hadjiconstantinou, and W. Wagner, "Low-noise Monte Carlo simulation of the variable hard-sphere gas," Phys. Fluids **23**, 030606 (2011).
[30] This conclusion is more clearly observed when analyzing the waveform in space at a given time (not presented here for brevity), and studying the gas response to boundary motion with shorter t_b, which better imitates sharp-impulse actuation.
[31] A. Manela and N. G. Hadjiconstantinou, "On the motion induced in a gas confined in a small-scale gap due to instantaneous boundary heating," J. Fluid Mech. **593**, 453–462 (2007).
[32] A. Manela and N. G. Hadjiconstantinou, "Gas-flow animation by unsteady heating in a microchannel," Phys. Fluids. **22**, 062001 (2010).
[33] D. Kalempa and F. Sharipov, "Sound propagation through a rarefied gas: Influence of the gas-surface interaction," Int. J. Heat Fluid Flow **38**, 190–199 (2012).